Interaction hot spots for phase separation revealed by NMR studies of a CAPRIN1 condensed phase

Tae Hun Kim[a,b,c,d], Brandon J. Payliss[b], Michael L. Nosella[b,d], Ian T. W. Lee[d], Yuki Toyama[a,b,c], Julie D. Forman-Kay[b,d,1], and Lewis E. Kay[a,b,c,d,1]

[a]Department of Molecular Genetics, University of Toronto, Toronto, ON M5S 1A8, Canada; [b]Department of Biochemistry, University of Toronto, Toronto, ON M5S 1A8, Canada; [c]Department of Chemistry, University of Toronto, Toronto, ON M5S 1A8, Canada; and [d]Program in Molecular Medicine, Hospital for Sick Children, Toronto, ON M5G 1X8, Canada

Edited by G. Marius Clore, NIH, Bethesda, MD, and approved April 22, 2021 (received for review March 12, 2021)

The role of biomolecular condensates in regulating biological function and the importance of dynamic interactions involving intrinsically disordered protein regions (IDRs) in their assembly are increasingly appreciated. While computational and theoretical approaches have provided significant insights into IDR phase behavior, establishing the critical interactions that govern condensation with atomic resolution through experiment is more difficult, given the lack of applicability of standard structural biological tools to study these highly dynamic large-scale associated states. NMR can be a valuable method, but the dynamic and viscous nature of condensed IDRs presents challenges. Using the C-terminal IDR (607 to 709) of CAPRIN1, an RNA-binding protein found in stress granules, P bodies, and messenger RNA transport granules, we have developed and applied a variety of NMR methods for studies of condensed IDR states to provide insights into interactions driving and modulating phase separation. We identify ATP interactions with CAPRIN1 that can enhance or reduce phase separation. We also quantify specific side-chain and backbone interactions within condensed CAPRIN1 that define critical sequences for phase separation and that are reduced by *O*-GlcNAcylation known to occur during cell cycle and stress. This expanded NMR toolkit that has been developed for characterizing IDR condensates has generated detailed interaction information relevant for understanding CAPRIN1 biology and informing general models of phase separation, with significant potential future applications to illuminate dynamic structure–function relationships in other biological condensates.

biomolecular condensates | intrinsically disordered protein regions | site-specific intermolecular interactions | modification of phase separation by ATP and *O*-GlcNAcylation | NMR methods for studying condensates

Biomolecular condensates have been implicated in an increasingly comprehensive array of biological processes (1). These condensates include, for example, membraneless organelles that control RNA processing (2), clusters of activated membrane receptors (3), signaling puncta (4), postsynaptic densities (5), and extracellular matrix materials (6). Recent predictions suggest that up to 80% of the components of the human proteome may be found in biological condensates at some stage of their lifetime, with half of these proteins driving phase separation (7). Condensates can create unique solvent environments to regulate enzymatic reactions (8, 9), exert mechanical pressure for remodeling lipid membranes (10), and support high local protein concentrations to facilitate the formation of fibers, both functional (11) and disease associated (12). These condensate solvent environments can also specifically enrich certain small molecule therapeutics to enable activity (13). The goal of structural biology to provide structure–function insights into normal biological or pathological processes and to support drug discovery meets a major challenge with condensates, due to their highly dynamic exchanging interactions, including those between intrinsically disordered protein regions (IDRs), folded protein binding domains, and nucleic acid elements (14). Understanding the role of specific residues in IDR phase separation to form dilute and condensed phases from a well-mixed solution and how IDR interactions differ between mixed and condensed states is necessary for illuminating the impact of the abundant, yet poorly understood, disease-causing mutations in IDRs (15) and for understanding how therapeutics may be specifically targeted to or excluded from the condensate solvent environment. Note that here, and in what follows, we refer to a dilute state as the low concentration phase in a phase-separated system and a mixed state as a non–phase-separated protein solution. X-ray crystallography, single particle electron cryomicroscopy, and NMR spectroscopy can be used to describe in detail stable structures with minimal dynamic excursions or with small numbers of discretely sampled states. While NMR can provide atomic-level information on highly dynamic systems such as those often found in condensed protein states, standard NMR approaches are often not easily applicable. In order to address the significant need for characterizing these systems, a limited number of NMR studies have been reported (16–18), yielding important insights into the nature of these states; however, methodological challenges remain.

Computational simulations (19, 20) and theoretical approaches (21) have provided more detailed pictures of interactions within these dynamic condensed phases. Powerful models of phase separation have identified certain residue types, primarily aromatics, as "stickers" within a context of "spacer" residues in order to explain phase behavior of various protein sequences (22). These

Significance

Many important biological processes occur within biomolecular condensates. Unlike many organelles, these condensates lack a surrounding membrane but are formed by phase separation due to interactions of their molecular components. Although the important role of intrinsically disordered protein regions (IDRs) in condensates is appreciated and contributing amino acids have been identified, experimentally derived site-specific information reporting on interactions between IDRs in condensed phases is lacking. Using a suite of NMR experiments with improved resolution and sensitivity for studies of condensed phases, we have obtained quantitative and site-specific information on interactions and hot spots that govern phase separation of the C-terminal IDR of CAPRIN1 and how phase separation can be modulated by posttranslational modifications, mutations, and interactions with ATP.

Author contributions: T.H.K., J.D.F.-K., and L.E.K. designed research; T.H.K., B.J.P., M.L.N., I.T.W.L., and L.E.K. performed research; T.H.K. and L.E.K. contributed new reagents/analytic tools; T.H.K., B.J.P., I.T.W.L., Y.T., and L.E.K. analyzed data; and T.H.K., J.D.F.-K., and L.E.K. wrote the paper.

The authors declare no competing interest.

This article is a PNAS Direct Submission.

[1]To whom correspondence may be addressed. Email: forman@sickkids.ca or kay@pound.med.utoronto.ca.

This article contains supporting information online at https://www.pnas.org/lookup/suppl/doi:10.1073/pnas.2104897118/-/DCSupplemental.

Published May 31, 2021.

models agree with a growing body of observations (23, 24), but more comprehensive validation requires additional information on specific contacts within the condensed state, preferably from ^{1}H-^{1}H nuclear Overhauser effects (NOEs), which are reporters of short-range contacts between pairs of interacting protons. In addition to determining the atomic-level details that contribute to phase separation, it is important to understand how adenosine triphosphate (ATP) can elicit variable effects, ranging from disruption or enhancement of condensation (25, 26). However, there is only limited site-specific experimental data on how ATP directly interacts with IDRs to mediate these behaviors.

In order to provide empirical data on specific interactions in the condensed phases of IDRs and to develop relevant NMR approaches that expand the toolkit for such studies, we have focused on a phase-separating IDR of CAPRIN1. This highly expressed RNA-binding protein found in many cytoplasmic condensates is involved in the regulation of messenger RNA (mRNA) translation and stability, is important for mechanisms underlying learning and memory, and has mutations associated with autism spectrum disorder (27, 28). We have previously shown that the C-terminal low-complexity IDR of CAPRIN1 (S607 to N709, hereafter referred to as CAPRIN1) phase separates in a manner that is dependent on salt and on interactions with RNA or FMRP (Fragile X mental retardation protein), another RNA-binding protein linked to neuronal function and to autism (17). Capitalizing on the small size (103 residues) that reduces spectral overlap, we have performed NMR studies on both CAPRIN1 and CAPRIN1/FMRP condensates, demonstrating that CAPRIN1 remains disordered and that interactions of both the arginine- and aromatic-rich regions are important for phase separation (17, 29).

Here, we have characterized the condensed state of CAPRIN1, developing NMR methodology in order to identify residues critical for CAPRIN1 phase separation and to understand the impact of posttranslational *O*-linked-*N*-acetylglucosaminylation (*O*-GlcNAcylation) of CAPRIN1 on its phase-separation properties. We show that moderate concentrations of ATP enhance phase separation by binding to the arginine-rich N- and C-terminal regions of CAPRIN1, whereas high concentrations of ATP lead to binding throughout the protein and inhibition of phase separation. Intermolecular NOEs within the condensed state, linking aliphatic and aromatic protons with backbone amide protons, are observed throughout the CAPRIN1 chain but are particularly strong for aromatic and H^{α} protons, highlighting the importance of backbone interactions in driving phase separation. In contrast, intramolecular NOEs in the condensed state are largely local. Our spin relaxation NMR data, coupled with mutagenesis, provide evidence of the correspondence between at least some of the intramolecular interactions in the dilute phase and intermolecular contacts in the condensed phase and, importantly, identify key hot spots in CAPRIN1 that form large numbers of interchain interactions leading to phase separation. *O*-GlcNAcylation, mutations, and ATP binding at high concentrations in the identified hot spot regions inhibit phase separation, underscoring the value of our NMR approaches in identifying the atomic- and residue-specific interactions involved in phase separation.

Results

ATP Binds to Arginine-Rich Regions of CAPRIN1, Increasing Phase Separation Propensity. CAPRIN1 contains 15 Arg residues, has a net charge of +13 at physiological pH, and an isoelectric point of 11.5. Previous studies have shown that it readily phase separates upon addition of salt or when negatively charged molecules, such as RNA, are added to screen electrostatic interactions between chains (17, 29). While ATP is considered to be a "hydrotrope" that can dissolve condensates (25) under certain conditions, we find that ATP promotes phase separation of CAPRIN1. Using ATP-Mg, since Mg^{2+} is required for ATP's biological activity (30), we identified CAPRIN1 and ATP-Mg concentrations that lead to formation of droplets (Fig. 1*A*, pink circles) and showed that CAPRIN1 and ATP are cophase separated in these droplets (Fig. 1*B*). Our results are consistent with other studies showing that ATP can enhance phase separation of some proteins, including FUS (26). In order to probe where ATP contacts the protein, we have recorded three-dimensional (3D) haCONHA NMR spectra [providing ^{13}CO, ^{15}N, and $^{1}H^{\alpha}$ correlations (29)] of 400 μM CAPRIN1 with 1.6 mM ATP-Mg added, concentrations that are sufficiently low so that sample turbidity is not observed and, therefore, extensive phase separation has not occurred. Although condensed droplets can be detected at these concentrations of protein and ATP-Mg (Fig. 1*B*) when using highly sensitive fluorescence imaging assays, the bulk of the protein is not phase separated, enabling the acquisition of high-quality NMR datasets on mixed-state protein samples. Replacement of a small fraction of ATP-Mg with ATP-Mn through the addition of 1% Mn^{2+} (relative to Mg^{2+}) leads to attenuation of cross peaks in spectra where binding occurs (Fig. 1*C*, black) due to paramagnetic relaxation enhancement of the amide proton signals caused by the unpaired electrons of Mn^{2+} (*SI Appendix*, Fig. S1). A Mn^{2+} control prepared in the absence of ATP shows that at the concentrations used in the present experiments free metal does not bind to CAPRIN1, as there is no spectral attenuation (green, Fig. 1*C*; reference *SI Appendix*). Notably, at these low concentrations of ATP, binding occurs in the Arg-rich N- and C-terminal regions of CAPRIN1, where the distribution of positive charge is highest, but not in the aromatic-rich central portion of the sequence (Fig. 1*C*). The localization of ATP-Mg to these regions is consistent with small chemical shift perturbations to spectra upon addition of ATP-Mg (*SI Appendix*, Fig. S1).

ATP-Mg Enhances CAPRIN1 Arginine, Aromatic, and Backbone Intermolecular Interactions. Having established that ATP-Mg enhances phase separation, we next sought to determine if intermolecular interactions in a mixed-state sample could be increased upon addition of low concentrations of ATP and if so which residues of CAPRIN1 would be involved. Such residues would then be expected to be among those important for phase separation. Residue-specific information on the contacts between molecules can be obtained by recording NOE spectra in which proton magnetization is transferred from a uniformly ^{13}C-labeled chain (black) to an unlabeled polypeptide (Fig. 2*A*). Because the NOE scales inversely with the sixth power of the distance between the interacting protons in each of the chains, the resulting cross peaks in these so-called edited-filtered nuclear Overhauser effect spectroscopy (NOESY) spectra (31) can provide residue-specific information on the strength of the time-averaged intermolecular contacts. A comparison of NOE spectra recorded with (red) and without (blue) 0.8 mM ATP-Mg (Fig. 2 *B*–*F*) establishes that certain interactions are strengthened upon addition of nucleotide. This is readily apparent in the increased NOE intensities reporting on Gly H^{α} (Fig. 2*B*), Arg H^{δ} (Fig. 2*D*), and non-Gly H^{α} (Fig. 2 *E* and *F*) interactions with aromatic side chains. Contacts connecting ATP with Gly, Arg, and aromatic residues are also observed. NOEs between aromatic residues in different chains are also present; these are strong even in the absence of ATP (Fig. 2*C*). The fact that many of the observed increases in NOE intensities report on interactions involving aromatic and arginine residues is consistent with previous studies showing that these amino acids are important for liquid–liquid phase separation (LLPS) of CAPRIN1 (17, 29) and other intrinsically disordered proteins (IDPs) or intrinsically disordered regions (IDRs) (22, 32, 33). Moreover, the increased intermolecular contacts between aromatic residues and the main chain upon addition of ATP (Fig. 2 *B*, *E*, and *F*) suggest an important but much less appreciated role for backbone interactions in promoting LLPS.

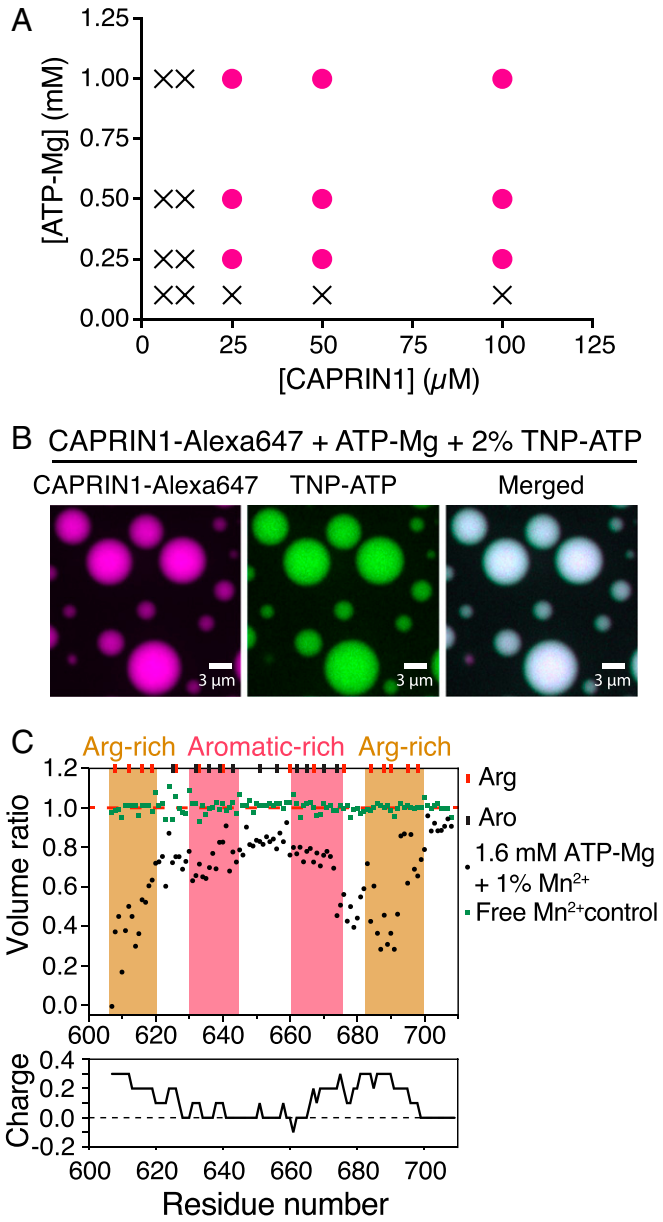

Fig. 1. Intermolecular CAPRIN1 interactions in the mixed state are enhanced by ATP. (*A*) Phase diagram mapping the formation of condensates as a function of ATP and CAPRIN1 concentration (25 °C); pink circles indicate conditions where condensates are formed. (*B*) ATP is enriched in the CAPRIN1 condensed phase, as established by fluorescence imaging experiments using 2% 2′-(or-3′)-*O*-(trinitrophenyl)-adenosine 5′-triphosphate (TNP-ATP) and CAPRIN1-Alexa647 (reference *SI Appendix* for details). The white bar in the lower right corner corresponds to a length of 3 μm. (*C*, *Top*) Volume ratios, V/V_o, of cross peaks in 3D haCONHA spectra (400 μM CAPRIN1, 25 mM HEPES, pH 7.4, 25 °C) where V_o is the peak volume in samples with 1.6 mM ATP-Mg, and V is the corresponding peak volume upon addition of 1% ATP-Mn (black). Control V/V_o ratios of peaks with (V) and without (V_o) Mn^{2+}, in the absence of ATP, are plotted in green (reference *SI Appendix* for details). Positions of Arg and aromatic residues are indicated by red and black ticks on the top edge of the panel, forming Arg- and aromatic-rich regions of sequence. (*Bottom*) Profile of the charge distribution of CAPRIN1, calculated by averaging charge over a sliding-window size of 10 residues.

NMR Experiments Probing Site-Specific Interactions in the Condensed Phase. ^{13}C-^{1}H NMR spectra of IDPs and IDRs of the sort presented in Fig. 2 are of modest utility because the assignment of interactions is largely limited to residue type only, due to poor chemical shift dispersion. Thus, although some information about contacts potentially important for LLPS can be obtained, these contacts, in general, cannot be ascribed to specific sites in the molecule. Therefore, we sought to develop NMR-based experiments of sufficient sensitivity and resolution to provide site-specific information on interactions between molecules in condensed protein phases. There are a number of factors that challenge such studies, including sample viscosity. A diffusion constant for CAPRIN1 of 1.6×10^{-8} cm^2/s at 35 °C was measured in the condensed phase (29), approximately two orders of magnitude slower than the corresponding diffusion rate in mixed-state samples. Similar ratios of diffusion constants of protein molecules in mixed state and condensed phases were reported for other protein systems (8, 18, 33). The slow tumbling and often conformational exchange leads to line broadening (*SI Appendix*, Fig. S2), and concomitant decreased spectral resolution relative to what can be achieved in studies of mixed-state samples, although often high-resolution solution-state spectra can still be recorded. Furthermore, the resulting fast signal decay challenges the utility of multidimensional experiments that combine recording of ^{15}N and ^{13}CO chemical shifts to improve spectral resolution (34). The problem of slow tumbling can be partially overcome by working at higher temperatures, leading to an increase both in overall rotation and in internal dynamics, so long as the chosen temperature is compatible with phase separation. The addition of NaCl to CAPRIN1 increases the upper critical solution temperature for phase separation (Fig. 3*A*). We chose to work at 400 mM NaCl and at a temperature of 40 °C; under these conditions, the concentration of protein in the condensed phase is 248 mg/mL or 22.4 mM.

As described above, a second challenging feature is an inability to resolve site-specific interactions. With this in mind, we chose to measure intermolecular NOEs between aliphatic or aromatic protons of one polypeptide chain and backbone amide protons of another, using a sample comprised of a combination of ^{12}C-, ^{15}N-, ^{2}H-labeled and ^{13}C-, ^{14}N-, ^{1}H-labeled chains, exploiting the excellent resolution of amide ^{15}N signals, even in IDPs and IDRs, to provide site-specific information. We have optimized the sensitivity and resolution in this class of experiments through the use of deuteration, which decreases signal decay and eliminates broadening due to unresolved ^{1}H scalar couplings. In the context of phase-separated proteins, the resolution and sensitivity enhancements can be significant (*SI Appendix*, Fig. S2). Fig. 3*B* presents a schematic of the NOE experiment used to quantify site-specific intermolecular interactions involving backbone amides in the condensed phase of CAPRIN1, in which contacts between protons coupled to ^{13}C (H^C) and ^{15}N (H^N) are recorded. The low natural abundance of ^{15}N (0.3%) effectively eliminates unwanted intramolecular NOEs between H^C and H^N pairs in the chain that is ^{13}C, ^{14}N in carbon and nitrogen, respectively, while the use of deuteration prevents the observation of intramolecular contacts in the ^{12}C, ^{15}N CAPRIN1 component. Note that the natural abundance of ^{13}C is 1.1% so that in a protonated ^{12}C, ^{15}N sample intrachain NOEs are likely to be observed in the absence of deuteration.

The comparative NOE experiments involving mixed-state samples with and without ATP (Fig. 2 *B*–*F*) highlight the importance of aromatic, Arg, and Gly residues as well as α-protons in forming interchain contacts in CAPRIN1. We have therefore developed a suite of NMR experiments to probe interactions between protein molecules in a condensed phase by measuring NOEs between amide protons on one chain and specific H^C protons on adjacent chains, from either aromatic or Arg (H^δ) side chains, or α-protons of either Gly or all residues except Gly. In an effort to evaluate the potential role of side-chain hydrogen bonding in CAPRIN1 LLPS, we have also developed an experiment that measures contacts between Ser residues (H^β) and backbone amides. As in previous studies by our groups (29, 33) and other laboratories (16, 18), phase-separated samples are prepared (NMR tube of Fig. 3*A*)

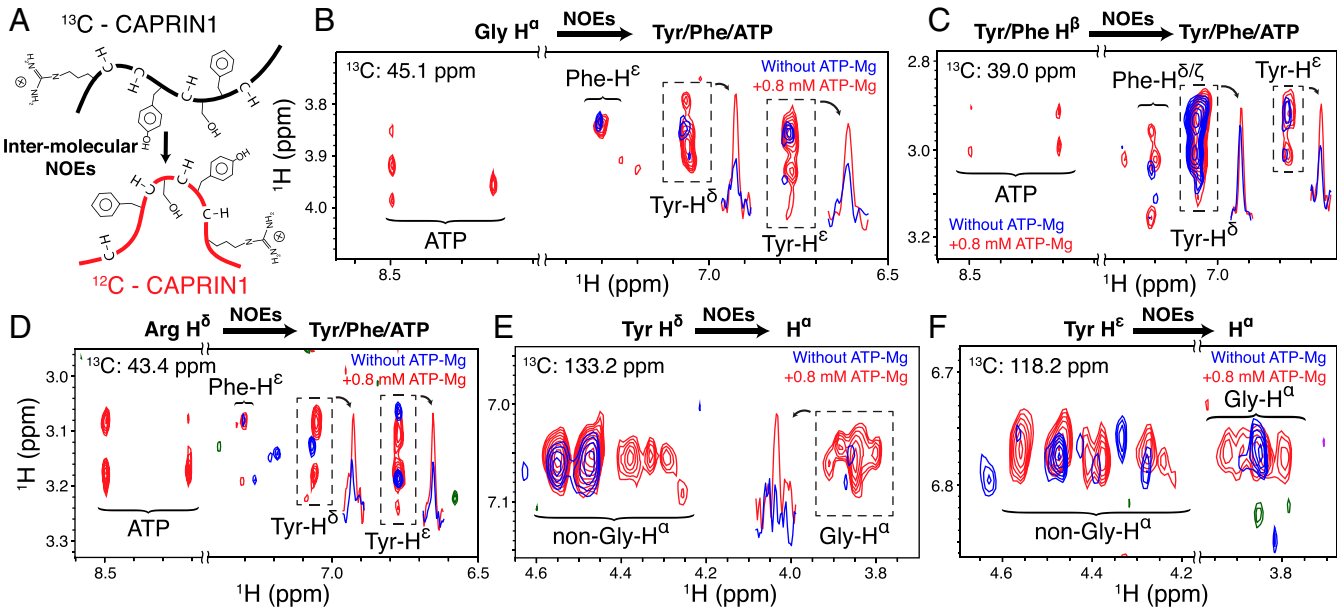

Fig. 2. ATP-Mg enhances CAPRIN1 intermolecular interactions. (*A*) Schematic of the magnetization flow in the ^{13}C-edited/filtered NOE experiment (31) used to measure intermolecular NOEs in mixed-state samples. In this application, both chains are protonated but only one is ^{13}C labeled. (*B–F*) Strips through a 3D ^{13}C-edited/filtered NOE dataset (250-ms mixing time, 25 °C, 0.5 mM ^{13}C-labeled + 0.5 mM ^{12}C-labeled CAPRIN1) highlighting particular contacts between adjacent CAPRIN1 chains (identified above each panel) without (blue) and with (red) 0.8 mM ATP-Mg. All NMR data were recorded at 600 MHz.

where the dilute protein phase is on top of the condensed phase and only the bottom region of the NMR sample is detected in experiments. Fig. 3*C* (black, *Top*) shows a ^{13}C-edited one-dimensional (1D) ^{1}H spectrum of the condensed phase of a phase-separated sample of ^{13}C-labeled CAPRIN1 prepared with a 1:2 ratio of ^{12}C-, ^{15}N-, ^{2}H:^{13}C-, ^{14}N-, and ^{1}H-labeled proteins. The 1D spectra below, along with the corresponding two-dimensional (2D) spectra of *SI Appendix*, Fig. S3, are those obtained by using selective editing and filtering strategies described in *SI Appendix* that isolate the indicated protons (H^{C}) in a manner that minimizes sensitivity losses, forming the basis for the five different intermolecular NOE experiments that have been developed. Magnetization from H^{C} is then transferred to amide positions on adjacent molecules to obtain interresidue correlations with site-specific resolution for the amides (*SI Appendix*, Fig. S4).

Fig. 3*D* highlights several spectral regions from a NOESY dataset showing aromatic (Phe and Tyr, as CAPRIN1 has no His or Trp) to amide intermolecular NOEs (red, 200-ms mixing time), superimposed on the corresponding regions from a regular HSQC-TROSY experiment (black). Note that this NOE spectrum and others like it (*SI Appendix*, Fig. S5) have the appearance of a ^{15}N-^{1}H^{N} HSQC correlation map, with the intensities of cross peaks providing a direct measure of the NOEs of interest, without artifacts from intramolecular correlations (*SI Appendix*, Fig. S6). Distinct differences are observed in NOE intensities. Strong intermolecular connectivities linking aromatic side-chain protons and many of the Gly H^{N} are found, including for G627, G334, and G338, that are located two amino acids C-terminal to an aromatic residue and whose amide correlations are significantly shifted upfield by ring currents. Intermolecular interactions linking aromatics from one chain with Arg amides from a second polypeptide are also observed in the aromatic-rich regions of the chains. Aromatic interactions with Gln residues are distinctly stronger than with Asn, while contacts involving Ser are weak (Fig. 3*D*). Gln residues have been shown to play important roles in protein aggregation associated with neurodegenerative disorders (35), and our data suggest that they are also significant for establishing contacts required in CAPRIN1 LLPS.

Strong intermolecular connectivities between aromatic side-chain and aromatic backbone protons are also observed. Previous work has noted the greater significance of Tyr than Phe in phase separation (22). Supporting these observations, NOEs from Tyr sidechains are considerably stronger than the corresponding connectivities from Phe (Fig. 3*E*), even after taking into account the fact that there are nearly twice as many Tyr as Phe residues in CAPRIN1 (seven versus four). *SI Appendix*, Fig. S5 highlights Arg to amide intermolecular NOEs. In general, Arg to aromatic amide correlations are strongest; however, there are significant site-specific variations.

NOE Hot Spots Highlight Important Regions for Phase Separation. 2D NOE spectra, similar to the aromatic dataset highlighted in Fig. 3*D*, have been recorded for other H^{C} protons that are illustrated in Fig. 3*C*. Fig. 4*A* shows 1D traces from the five experiments measuring intermolecular NOEs to H^{N} of Y662 and F643. Connectivities involving non-Gly H$^{\alpha}$ and aromatic protons are strongest, a trend that is observed for all of the residues. Intermolecular NOE intensities from each experiment connecting H^{C} protons with backbone amides (200 ms mixing time) are plotted as a function of residue in Fig. 4*B*, after first normalizing each NOE intensity to the corresponding intensity of the destination amide correlation in an HSQC dataset to account for residue-specific differences in peak intensities caused by relaxation effects and/or solvent exchange. The magnitudes of the normalized NOE values vary depending on the experiment. The strong intermolecular aromatic side-chain–H^{N} NOEs are consistent with the important role of aromatic residues in LLPS of aromatic-rich IDPs/IDRs (8, 22–24, 32, 33). Notably, within the aromatic experiment the residue-specific NOE intensities range significantly, with high values centered around residues G624-R626, G638-R640, and R660-Q666, in aromatic-rich regions of the sequence. Interchain NOE intensities derived from non-Gly H$^{\alpha}$–H^{N} interactions are also high, roughly twice as large as the aromatic NOEs, which likely reflects the twofold increase in the number of non-Gly α-protons (the number of protons is listed in the bottom right-hand corner). Interestingly, the NOE profiles

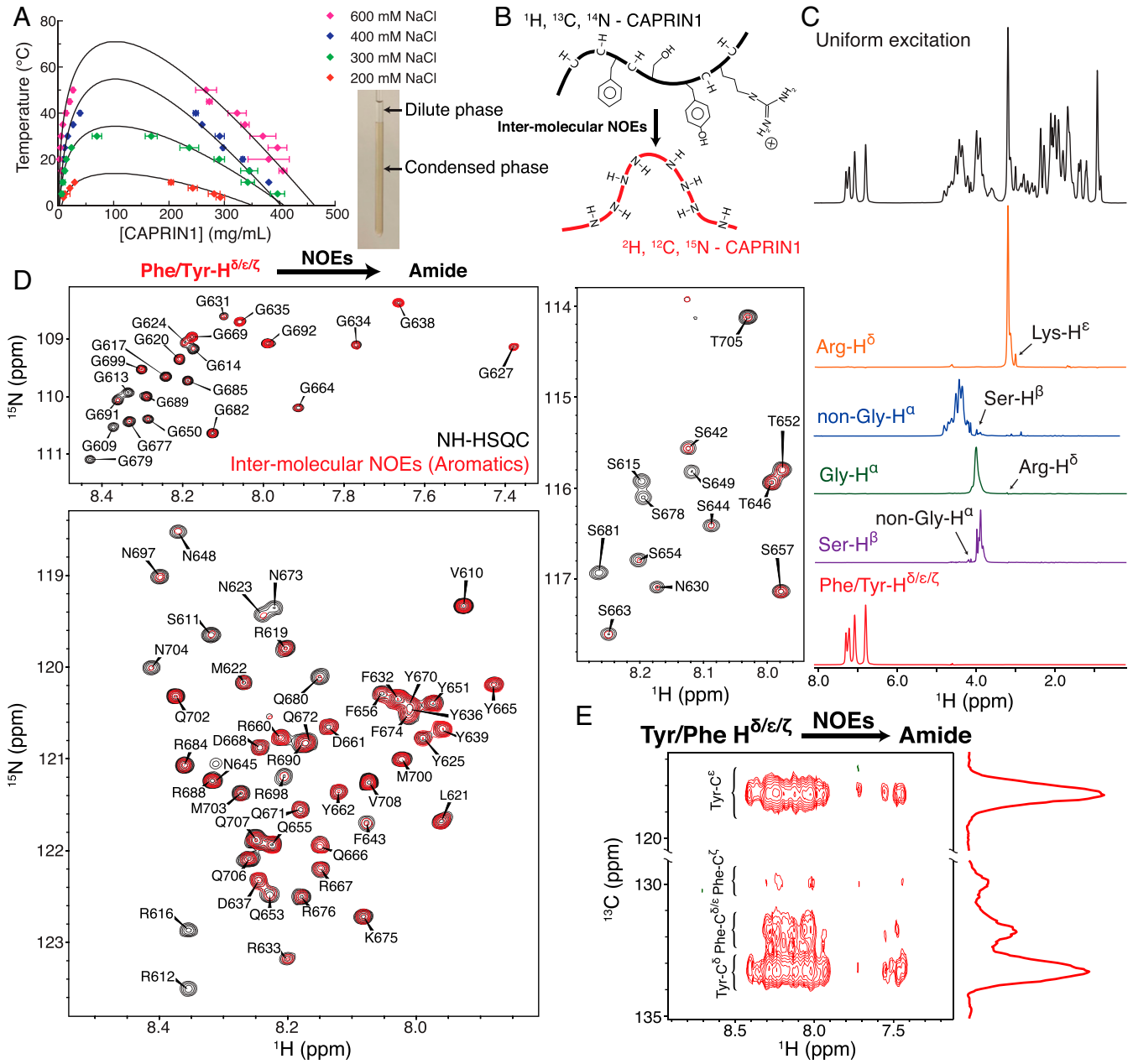

Fig. 3. Probing intermolecular interactions in the condensed CAPRIN1 phase. (*A*, *Left*) CAPRIN1 phase diagrams as a function of [NaCl], fit to a Flory–Huggins model (63, 64), as described previously (33) (solid lines). Error bars are SDs of triplicate measurements. (*Right*) NMR sample of phase-separated CAPRIN1, showing dilute (~39 mg/mL) and condensed (~250 mg/mL) phases. (*B*) Schematic of the intermolecular NOE experiment probing interactions with backbone amide protons, highlighting magnetization transfer between H^C and H^N. (*C*) ^{13}C-edited 1D ^{1}H spectra (40 °C, 1 GHz) of ^{13}C-labeled condensed phase CAPRIN1, selecting for protons (H^C), as indicated. The full ^{1}H spectrum is shown above. (*D*) Selected regions from a 200-ms NOE dataset showing aromatic to amide intermolecular NOEs (red), superimposed on the corresponding regions from an HSQC-TROSY spectrum (black), recorded at 1 GHz, 40 °C. (*E*) ^{13}C-$^1H^N$ NOE map (200 ms, 600 MHz, 40 °C) highlighting intermolecular contacts between aromatic and backbone amide protons. Note that correlations involving Tyr residues are significantly more intense than those from Phe.

for both experiments are similar, with maxima overlapping in both cases. Normalized NOE intensities for the remaining three experiments are smaller, in part reflecting the decreased numbers of Arg-H^δ and Ser-H^β protons, yet the profiles largely share the same positions of maxima (Fig. 4*B*). The sum of normalized NOE intensities from all experiments is also plotted, measured with mixing times of 100 and 200 ms, further highlighting regions of CAPRIN1 with increased intermolecular contacts in the condensed phase. Similar NOE profiles as those recorded with a 200-ms mixing time are observed for the 100-ms data, in which the effects of spin diffusion would be expected to be significantly reduced (*SI Appendix*, Fig. S7 and *Supplementary Information Text*). The two NOE profiles can be reasonably related through a scaling factor (Fig. 4*B*), although a perfect correlation would, of course, not be expected since one or both of the mixing times could well extend beyond the linear regime for at least some of the NOEs.

Having established that certain sequences of CAPRIN1 have enhanced interchain contacts, we were interested in testing whether these regions are important for LLPS. Noting that CAPRIN1

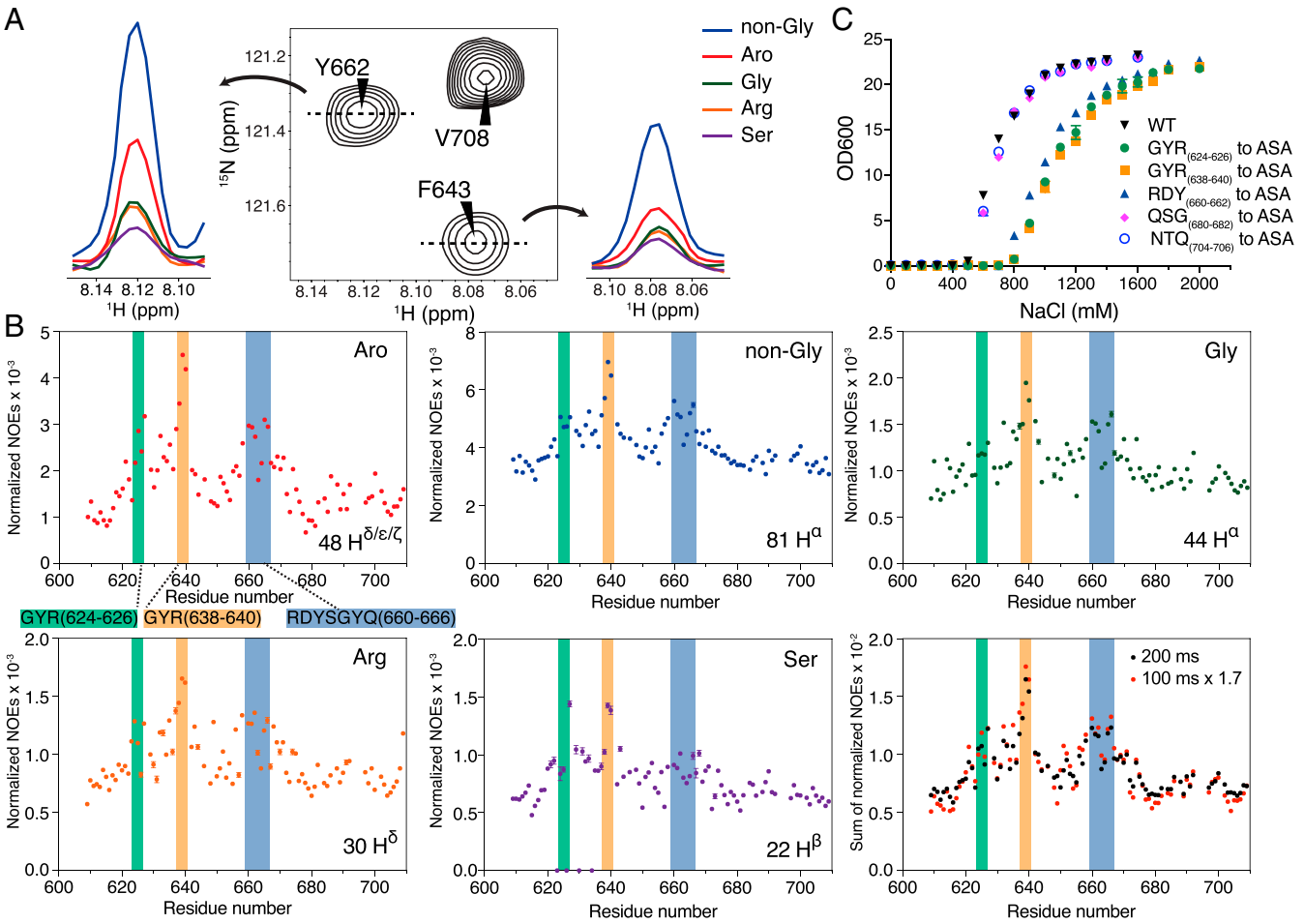

Fig. 4. Intermolecular NOE profiles highlight regions of preferred interactions in the condensed phase of CAPRIN1. (*A*) Comparative 1D traces from the five selective intermolecular NOE experiments (200-ms mixing time, 40 °C, 1 GHz), as indicated, focusing on contacts to H^N of Y662 and F643. (*B*) NOE profiles from each of the five selective experiments (Phe/Tyr $H^{\delta/\varepsilon/\zeta}$, non-Gly H^{α}, Gly H^{α} Arg H^{δ}, and Ser H^{β}), after normalizing NOE peak intensities to the intensities of the corresponding amide correlations in an HSQC-TROSY dataset. Both NOE and HSQC intensities are also normalized by the number of scans in each experiment. Regions of increased intensities are highlighted with green, orange, and blue stripes. The sum of NOE intensities from all five experiments (mixing times of 200 ms, black, and 100 ms, red) is shown. NOEs measured at the different mixing times show similar trends. (*C*) turbidity assays measuring LLPS propensities of 300-μM samples of CAPRIN1 as a function of [NaCl], 25 °C. Samples included WT and a series of mutants in which substitutions of three amino acid stretches to Ala-Ser-Ala (ASA) were made in regions predicted to drive phase separation and in the C terminus of the protein, as indicated. The measurements were performed in triplicate.

constructs with reduced LLPS propensities require higher concentrations of salt to phase separate to compensate for reduced interchain interactions, we performed turbidity assays that measure the light scattering accompanying LLPS as a function of NaCl concentration. Fig. 4*C* shows results from wild-type (WT) CAPRIN1 and a number of variants in which three-residue stretches were mutated to Ala-Ser-Ala in regions predicted to drive phase separation and in the C terminus of the protein, as controls, since the C terminus is expected to be less important based on a smaller number of intermolecular contacts. Our results indicate that mutations in regions with increased chain contacts significantly decrease CAPRIN1 LLPS.

Intramolecular Contacts in the Condensed Phase Are Local. The intermolecular NOE patterns (Fig. 4 and *SI Appendix*, Fig. S8, *Top*) show interactions extending over the complete CAPRIN1 chain, with preferences for specific regions of the sequence. In order to obtain information on intramolecular contacts, a phase-separated sample comprised of a 1:5 ratio of ^{13}C-, ^{15}N-, ^{1}H:^{12}C-, ^{14}N-, and ^{1}H-labeled molecules was prepared, and the same class of experiments as described above recorded. As both ^{13}C and ^{15}N isotope enrichments are localized to the same chain, intramolecular NOEs are expected to be much larger than their intermolecular counterparts highlighted in Fig. 4. Furthermore, the 1:5 ratio of isotopically enriched to unenriched molecules dilutes interactions between ^{13}C-, ^{15}N-, and ^{1}H-labeled chains, reducing intermolecular NOEs by ∼15-fold relative to what is observed in spectra recorded on 1:2 ^{12}C-, ^{15}N-, ^{2}H:^{13}C-, ^{14}N-, ^{1}H-labeled samples (*SI Appendix*). At this level of reduction, essentially all NOEs in spectra recorded on the 1:5 sample will be of the intramolecular variety. Fig. 5 *A*, *Left* shows normalized intramolecular NOE intensities for the aromatic and glycine datasets, showing distinct differences relative to the corresponding intermolecular NOE profiles (Fig. 4), which is further emphasized in *SI Appendix*, Fig. S8. For example, in the intramolecular NOE aromatic dataset, strong normalized NOE intensities, an order of magnitude larger than quantified for intermolecular NOEs (Fig. 4), are observed for correlations connecting aromatic side chains with H^N protons from aromatic residues (intraresidue, blue) or residues immediately following in sequence to aromatics (sequential, magenta). This trend, involving strong intraresidue or sequential NOEs is also noted in the other experiments, as illustrated for the

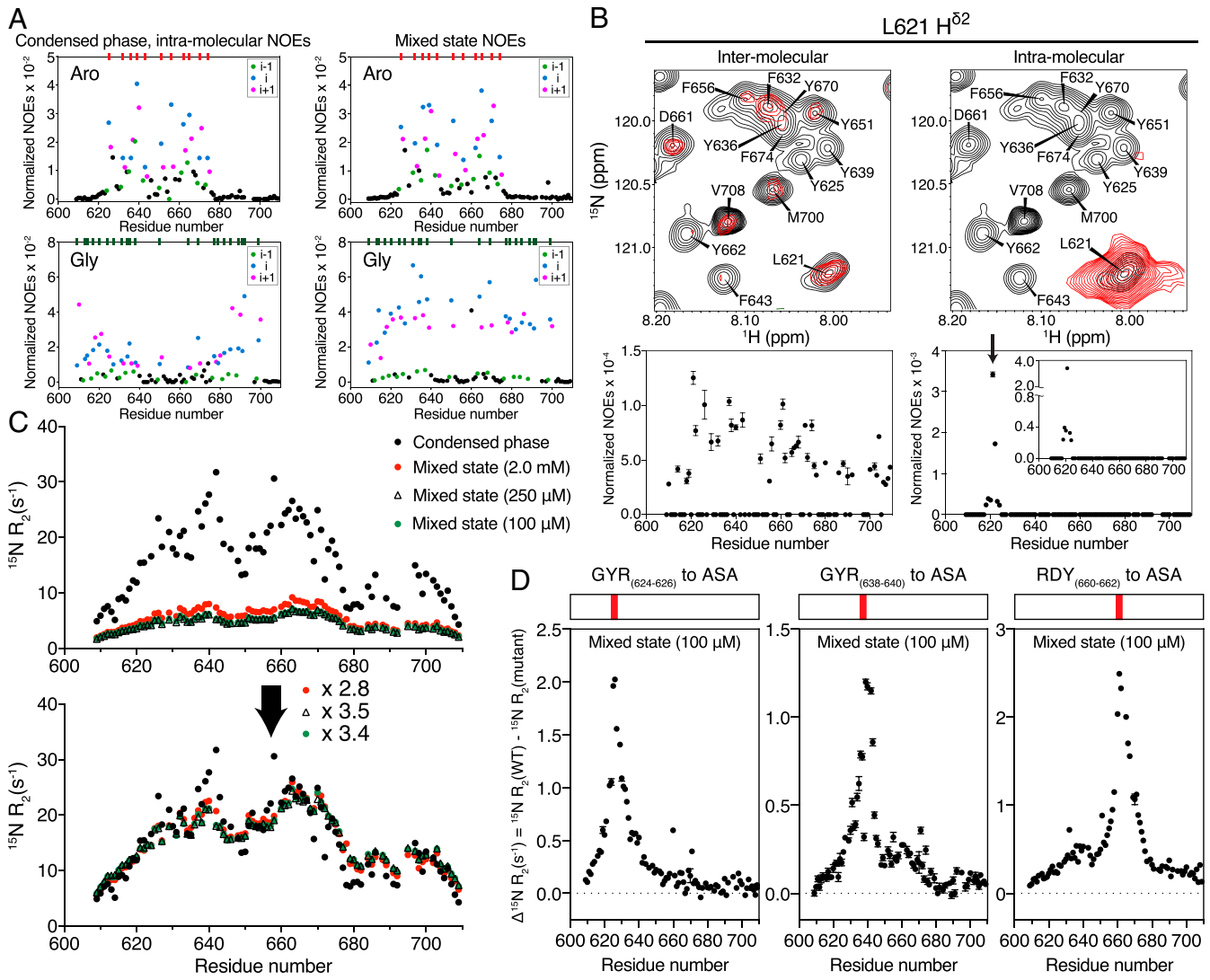

Fig. 5. Correspondence between intra- and interchain interactions in the mixed state and condensed phase, respectively. (*A*) Normalized intramolecular NOE intensities from aromatic (Aro) and glycine (Gly) datasets, with intraresidue and sequential correlations highlighted in blue and pink, respectively (200-ms mixing time, 40 °C, 1 GHz). (*B*, *Top*) Selected regions from 3D NOE datasets correlating proximal methyl and H^N protons (red), recorded on the condensed CAPRIN1 phase and focusing on corresponding planes connecting L621 $H^{\delta 2}$ and backbone H^N protons, in either an inter- (*Left*) or intra- (*Right*) molecular manner. Identical starting contour floors are used in both spectra. The black contours are those from an HSQC dataset. (*Bottom*) Profiles of NOE intensities, normalized to intensities of corresponding HSQC peaks, for inter- and intramolecular contacts between L621 $H^{\delta 2}$ and backbone H^N protons. Intensities of correlations from each of 3D NOE and 2D HSQC spectra were first normalized by measurement times of each dataset. An enlarged version for the intramolecular contacts is shown in *Inset*. (*C*, *Top*) ^{15}N R_2 profiles for the condensed CAPRIN1 phase, 40 °C (400 mM NaCl, 25 mM MES, pH 5.5, see *SI Appendix*; 600 MHz, black), and for 100-μM (green), 250-μM (open triangle), and 2-mM (red) concentrations of CAPRIN1 in the mixed state, 4 °C (25 mM MES, pH 5.5, see *SI Appendix*; 600 MHz). (*Bottom*) Profiles for the mixed-state samples have been multiplied by the values shown to best fit the condensed-phase data, reflecting the expected decrease in rates from the lowered viscosity due to smaller protein concentrations. (*D*) Plots of $\Delta R_2 = R_2(WT) - R_2(mutant)$ values measured on mixed-state samples of three of the mutants considered in Fig. 4*C*, with mutations centered in regions with increased intermolecular contacts in the condensed phase of CAPRIN1. In each case, three successive amino acids were mutated to Ala-Ser-Ala (ASA), as indicated. Data were recorded at 600 MHz, 4 °C.

profile showing Gly-H^{α}–H^N NOEs. Notably, similar profiles are also obtained for a mixed-state CAPRIN1 sample (Fig. 5 *A*, *Right*), with the large NOEs originating from intramolecular interactions. Differences between intra- and intermolecular chain contacts are also apparent in NOE profiles reporting site-specific interactions between methyl groups and backbone amides. Fig. 5*B* and *SI Appendix*, Fig. S9 show inter- and intramolecular NOE spectra (*Top*) connecting the methyl protons of L621 $H^{\delta 2}$ with proximal amide protons. Normalized NOE intensities are tabulated (*Bottom*), establishing that the intramolecular contacts are restricted primarily to intra- and sequential-residue correlations, while the intermolecular interactions extend more uniformly throughout the chain, linking L621 $H^{\delta 2}$ from one molecule with the amide proton of V708 from a neighboring CAPRIN1, for example (Fig. 5*B*). Similar results are obtained for other methyl–$^1H^N$ NOEs as well (*SI Appendix*, Fig. S9), and the wide distribution of intermolecular connectivities observed in a site-specific manner in the context of methyl-amide correlations is also noted. Notably, the absence of long-range intramolecular NOEs argues that spin diffusion along the ^{13}C-labeled chain is not responsible for the intermolecular NOE profiles observed. Rather, a picture emerges whereby adjacent chains make contact with each other throughout their lengths, with distinct preferences for interactions in certain regions, as identified here (Fig. 4*B*).

Correspondence between Intramolecular Interactions in a Mixed State and Intermolecular Interactions in a Condensed Phase. The measurement of intermolecular NOEs provides a direct way to quantify interactions between protein chains in the condensed phase. Insight can also be obtained by recording backbone ^{15}N transverse relaxation rates (R_2). ^{15}N R_2 values report the amplitudes and timescales of motion at each amide backbone position in the protein. Elevated relaxation rates within IDPs and IDRs are consistent with restrictions in motion on the picosecond to nanosecond, or slower, microsecond to millisecond timescales (*SI Appendix*, Fig. S2), reflecting interactions, either intra- or-intermolecular, that transiently stabilize structure to reduce conformational fluctuations. Fig. 5*C* (black) shows the ^{15}N R_2 profile for the condensed phase of CAPRIN1 (600 MHz). The pattern is highly correlated with those observed for profiles of mixed-state samples at different concentrations, which is made clear by scaling (that takes into account viscosity differences between samples) to superimpose these on the condensed-phase profile. The near superposition of ^{15}N R_2 profiles recorded for mixed-state CAPRIN1 samples over a 20-fold concentration range establishes that the fine structure in these rates derives from intrachain interactions (Fig. 5*C*). The strong correlation between mixed-state and condensed-phase R_2 profiles implies that at least some of the interactions that restrict CAPRIN1 dynamics are conserved within condensed and mixed-state samples. In order to establish whether some of the intramolecular contacts in the mixed state, responsible for the R_2 pattern, convert to intermolecular interactions in the condensed phase, we recorded ^{15}N R_2 rates of mixed-state CAPRIN1 samples with mutations centered in regions showing large NOE contacts (Fig. 4). Fig. 5*D* shows $\Delta R_2 = R_2(\text{WT}) - R_2(\text{mutant})$ values for the three mutants considered in Fig. 4*C* that affect phase separation, showing significantly decreased R_2 values in the vicinity of the mutation site in each case, reflecting decreased transient intrachain interactions. These mutations are associated with decreases in phase separation propensity and hence elimination of important intermolecular contacts promoting LLPS, suggesting a correspondence between CAPRIN1 intramolecular interactions in the mixed state and intermolecular contacts in the condensed phase.

***O*-GlcNAcylation of CAPRIN1 and High ATP-Mg Concentration Reduces Phase Separation Propensity.** Recent studies indicate that CAPRIN1, together with other stress-granule–forming proteins such as FUS, is posttranslationally modified by *O*-GlcNAcylation (36). In the case of CAPRIN1, *O*-GlcNAc levels decrease as quiescent MCF-7 cells progress toward S phase (37) and increase in mouse embryonic fibroblasts as part of an acute oxidative stress response (36). Despite the potential functional significance of CAPRIN1 *O*-GlcNAcylation, sites of glycosylation in the C-terminal IDR are not known, nor its impact on phase behavior. We have used NMR to monitor the progression of in vitro *O*-GlcNAcylation of CAPRIN1 by *O*-GlcNAc transferase (OGT), showing that both S644 and S649 become glycosylated, with S644 modified more rapidly (Fig. 6*A* and *SI Appendix*, Fig. S10). Of note, S644 is proximal to the GYR sequence comprising residues 638 to 640 (Fig. 6*A*), an interaction hot spot with increased normalized intermolecular NOE intensities (Fig. 4*B*) and enhanced ^{15}N R_2 rates (Fig. 5*C*) that we observe to be important for LLPS (Fig. 4*C*). Not surprisingly, therefore, *O*-GlcNAcylation decreases the tendency of CAPRIN1 to phase separate, relative to the unmodified protein (Fig. 6*B*).

Having established that glycosylation at a site proximal to those important for phase separation reduces CAPRIN1's propensity to phase separate, we wondered if the addition of high concentrations of ATP-Mg, which was previously shown to promote reentrance into a mixed state (i.e., dissolve condensates) (25, 26), might similarly bind to regions of CAPRIN1 that drive phase separation. Fig. 6*C* profiles the concentration of ATP-Mg over which phase separation of a 400 μM CAPRIN1 solution occurs (monitored by high OD_{600}), showing reentrance to a mixed state at a nucleotide concentration of ∼45 mM. We, therefore, measured intensities of correlations in 3D haCONHA spectra recorded with 70 mM ATP-Mg + 1% Mn^{2+} (black) or without ATP-Mg (green) (Fig. 6*D*). Peak broadening across the protein establishes that ATP-Mg at 70 mM binds to both Arg- and aromatic-rich regions of CAPRIN1. Thus, the high concentrations of ATP, similar to *O*-GlcNAcylation at S644 and S649, can decrease CAPRIN1 phase-separation propensity by affecting the aromatic-rich hot spots for phase separation, with the addition of excess negative charge by ATP-Mg also likely playing a significant role.

Discussion

A prerequisite for understanding protein phase separation involves identifying and quantifying intermolecular interactions between protein chains at the atomic level. As a first step, mutagenesis studies have focused on establishing key residue types that are important for LLPS. These include aromatic residues for the N-terminal low-complexity regions (LCRs) of the germ granule protein Ddx4 and the RNA granule protein FUS whose phase-separation propensities are reduced by mutation of Phe (Ddx4) (8) and by mutation of Tyr residues in repetitive SYGQ motifs (FUS) (24, 32). The importance of Arg residues has been recognized through arginine methylation studies of Ddx4, FMRP, FUS, and hnRNPA2 LCRs in vitro (8, 38–40) and of FUS in cells (41, 42), as well as by Arg-to-Lys mutational analyses of Ddx4 (33), FMRP (38), CAPRIN1 (29), FUS (22, 42), and hnRNPA1 (22). Notably, the phase-separation propensities of proteins of the FUS family, which contain prion-like domains (PLDs) such as the FUS N-terminal LCR, have been found to be correlated with the numbers of Arg and Tyr residues in the sequence (22), emphasizing the importance of these residues for LLPS in this system.

Several theoretical studies have provided evidence that the same types of interactions responsible for compaction of the chain in mixed-state samples play an important role in promoting LLPS (43, 44). Consistent with this notion, experimental studies on a set of synthetic PLDs derived from hnRNPA1 in which the number of aromatic amino acids was varied have shown that both chain compactness and phase-separation propensity correlate with the numbers and positions of these residues (23). The formation of transient interactions involving side chains of these "stickers" promotes LLPS, while the hydrated "spacers" between them moderate interchain interactions so as to prevent aggregation. This sticker-spacer model has been used to accurately predict phase diagrams of PLD variants from hnRNPA1 (23), providing crucial and quantitative insights into the sort of interactions that govern LLPS. In addition, electrostatic interactions, including effects of charge patterning and phosphorylation, are also significant (8, 38, 45), and theoretical models have been successful in predicting general phase behavior in a number of cases (21, 22, 46, 47). However, chemical groups beyond Tyr, Phe, Arg, and other charged side chains also play important roles, as evidenced by the high phase-separation propensity of poly-Gln stretches (48) and of elastin (49), which has almost no aromatics or charged amino acids, and by the enrichment of Gly, Ser, and other residues within phase-separating LCRs. Despite an improved understanding of what amino acids drive LLPS in different protein systems, experimentally derived site-specific information reporting on interactions between protein molecules in condensed phases is still needed but has remained challenging to obtain. In principle, such data are available from NMR studies of condensed protein phases. In practice, however, poor resolution, peak broadening, and often low-complexity amino acid sequences of the proteins that are typically studied lead to difficulties in measuring site-specific dynamics or structural parameters. Thus, while interactions

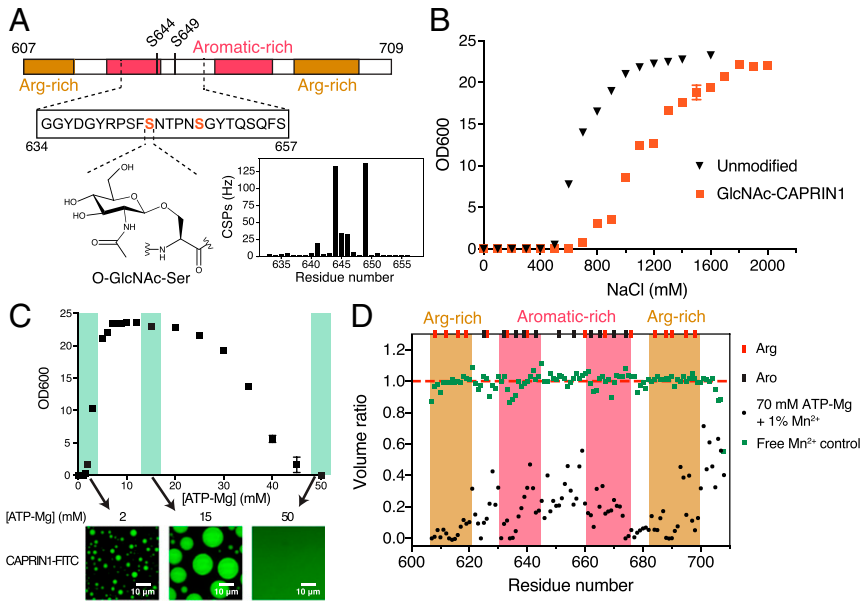

Fig. 6. Modulation of CAPRIN1 phase separation by *O*-GlcNAcylation or addition of ATP-Mg. (*A*) *O*-GlcNAcylation occurs at both S644 and S649 of CAPRIN1, with the former site proximal to a region with a large number of interchain contacts in the condensed phase. A series of 3D haCONHA experiments (29) was recorded to quantify the progress of CAPRIN1 glycosylation upon addition of ^{15}N,^{13}C CAPRIN1, UDP-GlcNAc, and the enzyme OGT, 25 °C. Chemical shift perturbations (CSP), CSP = $\sqrt{\sum \Delta\nu_i^2}$, where $\Delta\nu_i$ is the difference (Hz) between peak positions in haCONHA datasets recorded prior to and after 33 h of the GlcNAcylation reaction; the sum is over {^{1}H$^\alpha$, ^{13}CO, ^{15}N} shifts. (*B*) Turbidity assays comparing the LLPS propensity of unmodified and GlcNAc-modified CAPRIN1 (300 μM) as a function of [NaCl], 25 °C. (*C*, *Top*) Turbidity assays measuring LLPS propensity of CAPRIN1 (400 μM) as a function of [ATP-Mg]. Turbidity measurements in (*B*) and (*C*, *Top*) were performed in triplicate, with error bars representing 1 SD usually smaller than the plotted symbols. (*Bottom*) Fluorescence images recorded at indicated ATP concentrations showing phase separation ([ATP-Mg] = 2 mM, 15 mM) or reentrance into a mixed state ([ATP-Mg] = 50 mM). The white bars correspond to 10 μm. (*D*) Volume ratios of correlations in haCONHA spectra (V/V_o), 25 °C, recorded with 70 mM ATP-Mg and with (V) or without (V_o) 1% Mn^{2+}, in black, or with (V) and without (V_o) Mn^{2+} in the absence of ATP, as a control in green (*SI Appendix*).

could be assigned to residue types based on analyses of NOE spectra recorded on condensed phases of LCRs of Ddx4 (33) and FUS (18)—showing in the case of FUS, that interactions involving all residues of SYGQ-rich sequences are important for LLPS and for both proteins that multiple contacts connecting different residue types are present—in general, site-specific assignments of NOE data were lacking. In addition, relaxation rates (16, 33, 50), providing site-specific details of molecular dynamics, or hydrogen exchange rates that quantify dynamics on slower timescales (51) could only be obtained for approximately half of the residues in Ddx4 and FUS LCRs, limiting any conclusions that could be made.

Here, using a 103-residue CAPRIN1 LCR fragment as a model system for which well-resolved 2D ^{15}N-^{1}H^N spectra are recorded at a magnetic field strength of 23.4 T (1 GHz), we have designed and applied sensitive 2D NOE-based experiments providing contacts between selected aromatic or aliphatic protons and backbone amide protons. Both intra- and intermolecular interactions were recorded within and between CAPRIN1 molecules, respectively, in the condensed phase. Samples comprising combinations of highly deuterated (as opposed to protonated) ^{15}N-labeled chains and protonated, ^{13}C-labeled chains were used to record intermolecular NOEs, removing potential intramolecular NOE artifacts (*SI Appendix*, Fig. S6), and to increase spectral resolution and sensitivity (*SI Appendix*, Fig. S2). The results obtained provide nuanced and quantitative data to inform and validate various models of phase separation, as well as specific details regarding CAPRIN1 condensation relevant to its biological function. For example, while our study highlights the importance of aromatic side chains in promoting interchain interactions, as observed previously both in this system (17) and in other proteins (22, 23, 32), it establishes that H$^\alpha$-H^N contacts are significant as well (Fig. 4*B*). Notably, a similar pattern of NOE intensities is observed across all experiments, but particularly for the aromatic and H$^\alpha$ datasets, and although contacts between chains are extensive, they are strongest in the aromatic-rich regions of sequence. While transient kinked β-structure has been suggested to be important for phase separation of PLDs of FUS and related family members (24, 52), the general role of backbone interactions in LLPS has not been fully appreciated; these may be stabilized through amide hydrogen bonding and/or π interactions, giving rise to the H$^\alpha$-H^N NOEs measured here. Hydrogen-bonding interactions have been observed in molecular dynamics simulations of elastin-like peptides (53) and hydrogen bonds and π–π interactions noted in simulations of the LCR of FUS (18). Our intermolecular NOE profiles also indicate three areas that appear to be of particular importance for LLPS of CAPRIN1 (Fig. 4*B*), based on the numbers of contacts in each of these regions. The observed intermolecular NOE patterns were distinct from those for intramolecular NOEs, with the latter dominated by intraresidue correlations or those connecting sequential residues (Fig. 5*A* and *SI Appendix*, Figs. S8 and S9).

Key regions in CAPRIN1 identified from measured intermolecular NOEs as important for LLPS also show elevated backbone ^{15}N R_2 relaxation rates. Higher R_2 rates, similar to NOEs, provide a fingerprint of regions of the polypeptide chain making transient contacts, based on reduction of the dynamic conformational sampling that occurs in IDRs/IDPs (54). Notably, replacement of three consecutive amino acids in these key sequences by Ala-Ser-Ala significantly decreases phase separation propensities (Fig. 4*C*) and reduces the elevated R_2 rates in mixed samples (Fig. 5*D*). Our data support at least a partial correspondence between intra- and interchain interactions in the mixed state and condensed phase of CAPRIN1, respectively, and additionally demonstrate that interactions involving both aromatic and H$^\alpha$ protons are especially important in LLPS.

Posttranslational modifications (PTMs) of proteins regulate a plethora of different biological functions, including cell-cycle progression, apoptosis, and RNA translation (55, 56). Phosphorylation-dependent phase separation of CAPRIN1 and FMRP control mRNA translation and deadenylation rates in vitro (17), corresponding to reported cellular phosphoregulation of these processes (57). The impact of PTMs on phase separation of numerous LCRs has been demonstrated for phosphorylation and arginine methylation (8, 38, 58), with many fewer reports for *O*-GlcNAcylation (59). Our investigation of *O*-GlcNAcylation of CAPRIN1, showing two sites of glycosylation with the principal site proximal to an NOE hot spot region of the protein, suggests a specific effect of this PTM in blocking key favorable interactions that mediate LLPS. Our results shed light on how tuning *O*-GlcNAc levels may contribute to the assembly and disassembly of CAPRIN1-containing cytoplasmic RNA bodies in normal biology in response to cell-cycle progression or oxidative stress (36, 37). In addition, they motivate future studies of the roles of *O*-GlcNAc in disease, given that dysregulation of the assembly and disassembly dynamics of CAPRIN1-containing stress granules and neuronal mRNA transport granules are associated with amyotrophic lateral sclerosis (ALS) and autism spectrum disorders, respectively (28, 60).

While low-complexity IDR sequences cannot typically be aligned by position, many features within them are conserved and are likely to be significant for their phase behavior (61, 62), including the number and distribution of charges and key residue types, and of sites for PTMs and for binding partners. Our results, highlighting NOE hot spots critical for phase separation along the protein backbone, and together with NMR studies of a more qualitative nature (18, 29, 33), underscore the contributions from multiple side chains and, importantly, in this work, from backbone groups, to LLPS. While atomistic representations of ensembles of IDRs within condensed phases based on molecular dynamics and simulation approaches have been described, these can be validated and more confident descriptions of condensates obtained by using site-specific NOEs, such as those obtained in the present study, that are of particular value due to their strong dependence on short distances. The methods described here extend the NMR toolkit for characterization of IDR condensates and represent steps forward for establishing site-specific determinants that govern their formation and for generating data for experimentally driven atomistic ensemble descriptions of these dynamic states that underlie a range of biological processes.

Materials and Methods

CAPRIN1 and OGT were expressed in *Escherichia coli* BL21 (DE3) RIPL cells and purified using Ni-NTA column (GE Healthcare) and size exclusion chromatography. Details of NMR experiments, turbidity assays, fluorescence imaging, construction of the phase diagrams, and of the *O*-GlcNAcylation reaction are provided in *SI Appendix*.

Data Availability. All study data are included in the article and/or *SI Appendix*.

ACKNOWLEDGMENTS. T.H.K. is supported by a Banting postdoctoral fellowship from the Canadian Institutes of Health Research (CIHR) and the H. L. Holmes Award from the National Research Council of Canada. M.L.N. acknowledges an Alexander Graham Bell Canada Graduate Doctoral Scholarship from the Natural Sciences and Engineering Research Council of Canada (NSERC). Y.T. is a recipient of the Overseas Research Fellowship from the Japan Society for the Promotion of Science. This research was funded by CIHR Grants FDN-503573 (L.E.K.), FND-148375 (J.D.F.-K.), NSERC Grants 2015-04347 (L.E.K.), 2016-06718 (J.D.F.-K.), and NIH Grant 5R01GM127627-03 (J.D.F.-K.). L.E.K. and J.D.F.-K. were supported by the Canada Research Chairs Program. We thank the SickKids Imaging Facility for their assistance with the microscopy experiments and acknowledge the use of the SickKids Structural and Biophysical Core Facility. Dr. T. Reid Alderson is acknowledged for critically reading the manuscript.

1. S. F. Banani, H. O. Lee, A. A. Hyman, M. K. Rosen, Biomolecular condensates: Organizers of cellular biochemistry. *Nat. Rev. Mol. Cell Biol.* **18**, 285–298 (2017).
2. Y. S. Mao, B. Zhang, D. L. Spector, Biogenesis and function of nuclear bodies. *Trends Genet.* **27**, 295–306 (2011).
3. X. Su *et al*., Phase separation of signaling molecules promotes T cell receptor signal transduction. *Science* **352**, 595–599 (2016).
4. J. Z. Zhang *et al*., Phase separation of a PKA regulatory subunit controls cAMP compartmentation and oncogenic signaling. *Cell* **182**, 1531–1544.e15 (2020).
5. M. Zeng *et al*., Phase transition in postsynaptic densities underlies formation of synaptic complexes and synaptic plasticity. *Cell* **166**, 1163–1175.e12 (2016).
6. L. D. Muiznieks, S. Sharpe, R. Pomès, F. W. Keeley, Role of liquid-liquid phase separation in assembly of elastin and other extracellular matrix proteins. *J. Mol. Biol.* **430**, 4741–4753 (2018).
7. M. Hardenberg, A. Horvath, V. Ambrus, M. Fuxreiter, M. Vendruscolo, Widespread occurrence of the droplet state of proteins in the human proteome. *Proc. Natl. Acad. Sci. U.S.A.* **117**, 33254–33262 (2020).
8. T. J. Nott *et al*., Phase transition of a disordered nuage protein generates environmentally responsive membraneless organelles. *Mol. Cell* **57**, 936–947 (2015).
9. J. Sheu-Gruttadauria, I. J. MacRae, Phase transitions in the assembly and function of human miRISC. *Cell* **173**, 946–957.e16 (2018).
10. L. P. Bergeron-Sandoval *et al*., Endocytosis caused by liquid-liquid phase separation of proteins. *bioRxiv* [Preprint] (2017). https://doi.org/10.1101/145664 (Accessed 24 May 2021).
11. Y. Lin *et al*., Toxic PR poly-dipeptides encoded by the C9orf72 repeat expansion target LC domain polymers. *Cell* **167**, 789–802.e12 (2016).
12. A. Patel *et al*., A liquid-to-solid phase transition of the ALS protein FUS accelerated by disease mutation. *Cell* **162**, 1066–1077 (2015).
13. I. A. Klein *et al*., Partitioning of cancer therapeutics in nuclear condensates. *Science* **368**, 1386–1392 (2020).
14. H. Y. J. Fung, M. Birol, E. Rhoades, IDPs in macromolecular complexes: The roles of multivalent interactions in diverse assemblies. *Curr. Opin. Struct. Biol.* **49**, 36–43 (2018).
15. A. K. Dunker *et al*., Intrinsically disordered protein. *J. Mol. Graph. Model.* **19**, 26–59 (2001).
16. K. A. Burke, A. M. Janke, C. L. Rhine, N. L. Fawzi, Residue-by-residue view of in vitro FUS granules that bind the C-terminal domain of RNA polymerase II. *Mol. Cell* **60**, 231–241 (2015).
17. T. H. Kim *et al*., Phospho-dependent phase separation of FMRP and CAPRIN1 recapitulates regulation of translation and deadenylation. *Science* **365**, 825–829 (2019).
18. A. C. Murthy *et al*., Molecular interactions underlying liquid-liquid phase separation of the FUS low-complexity domain. *Nat. Struct. Mol. Biol.* **26**, 637–648 (2019).
19. K. M. Ruff, R. V. Pappu, A. S. Holehouse, Conformational preferences and phase behavior of intrinsically disordered low complexity sequences: Insights from multiscale simulations. *Curr. Opin. Struct. Biol.* **56**, 1–10 (2019).
20. S. Das, Y. H. Lin, R. M. Vernon, J. D. Forman-Kay, H. S. Chan, Comparative roles of charge, π, and hydrophobic interactions in sequence-dependent phase separation of intrinsically disordered proteins. *Proc. Natl. Acad. Sci. U.S.A.* **117**, 28795–28805 (2020).
21. Y. H. Lin, J. D. Forman-Kay, H. S. Chan, Sequence-specific polyampholyte phase separation in membraneless organelles. *Phys. Rev. Lett.* **117**, 178101 (2016).
22. J. Wang *et al*., A molecular grammar governing the driving forces for phase separation of prion-like RNA binding proteins. *Cell* **174**, 688–699.e16 (2018).
23. E. W. Martin *et al*., Valence and patterning of aromatic residues determine the phase behavior of prion-like domains. *Science* **367**, 694–699 (2020).
24. M. Kato *et al*., Cell-free formation of RNA granules: Low complexity sequence domains form dynamic fibers within hydrogels. *Cell* **149**, 753–767 (2012).
25. A. Patel *et al*., ATP as a biological hydrotrope. *Science* **356**, 753–756 (2017).
26. J. Kang, L. Lim, Y. Lu, J. Song, A unified mechanism for LLPS of ALS/FTLD-causing FUS as well as its modulation by ATP and oligonucleic acids. *PLoS Biol.* **17**, e3000327 (2019).
27. K. Nakayama *et al*., RNG105/caprin1, an RNA granule protein for dendritic mRNA localization, is essential for long-term memory formation. *eLife* **6**, 489 (2017).
28. Y. H. Jiang *et al*., Detection of clinically relevant genetic variants in autism spectrum disorder by whole-genome sequencing. *Am. J. Hum. Genet.* **93**, 249–263 (2013).
29. L. E. Wong, T. H. Kim, D. R. Muhandiram, J. D. Forman-Kay, L. E. Kay, NMR experiments for studies of dilute and condensed protein phases: Application to the phase-separating protein CAPRIN1. *J. Am. Chem. Soc.* **142**, 2471–2489 (2020).
30. J. H. F. de Baaij, J. G. J. Hoenderop, R. J. M. Bindels, Magnesium in man: Implications for health and disease. *Physiol. Rev.* **95**, 1–46 (2015).
31. C. Zwahlen *et al*., Methods for measurement of intermolecular NOEs by multinuclear NMR spectroscopy: Application to a bacteriophage λ N-peptide/boxB RNA complex. *J. Am. Chem. Soc.* **119**, 6711–6721 (1997).
32. Y. Lin, S. L. Currie, M. K. Rosen, Intrinsically disordered sequences enable modulation of protein phase separation through distributed tyrosine motifs. *J. Biol. Chem.* **292**, 19110–19120 (2017).
33. J. P. Brady *et al*., Structural and hydrodynamic properties of an intrinsically disordered region of a germ cell-specific protein on phase separation. *Proc. Natl. Acad. Sci. U.S.A.* **114**, E8194–E8203 (2017).
34. W. Bermel, I. Bertini, I. C. Felli, R. Kümmerle, R. Pierattelli, Novel ^{13}C direct detection experiments, including extension to the third dimension, to perform the complete assignment of proteins. *J. Magn. Reson.* **178**, 56–64 (2006).
35. H. Y. Zoghbi, H. T. Orr, Glutamine repeats and neurodegeneration. *Annu. Rev. Neurosci.* **23**, 217–247 (2000).

36. A. Lee *et al*., Combined antibody/lectin enrichment identifies extensive changes in the O-GlcNAc sub-proteome upon oxidative stress. *J. Proteome Res.* **15**, 4318–4336 (2016).
37. L. Drougat *et al*., Characterization of O-GlcNAc cycling and proteomic identification of differentially O-GlcNAcylated proteins during G1/S transition. *Biochim. Biophys. Acta* **1820**, 1839–1848 (2012).
38. B. Tsang *et al*., Phosphoregulated FMRP phase separation models activity-dependent translation through bidirectional control of mRNA granule formation. *Proc. Natl. Acad. Sci. U.S.A.* **116**, 4218–4227 (2019).
39. V. H. Ryan *et al*., Mechanistic view of hnRNPA2 low-complexity domain structure, interactions, and phase separation altered by mutation and arginine methylation. *Mol. Cell* **69**, 465–479.e7 (2018).
40. T. Yoshizawa *et al*., Nuclear import receptor inhibits phase separation of FUS through binding to multiple sites. *Cell* **173**, 693–705.e22 (2018).
41. S. Qamar *et al*., FUS phase separation is modulated by a molecular chaperone and methylation of arginine cation-π interactions. *Cell* **173**, 720–734.e15 (2018).
42. M. Hofweber *et al*., Phase separation of FUS is suppressed by its nuclear import receptor and arginine methylation. *Cell* **173**, 706–719.e13 (2018).
43. Y. H. Lin, H. S. Chan, Phase separation and single-chain compactness of charged disordered proteins are strongly correlated. *Biophys. J.* **112**, 2043–2046 (2017).
44. T. S. Harmon, A. S. Holehouse, M. K. Rosen, R. V. Pappu, Intrinsically disordered linkers determine the interplay between phase separation and gelation in multivalent proteins. *eLife* **6**, e30294 (2017).
45. H. Lu *et al*., Phase-separation mechanism for C-terminal hyperphosphorylation of RNA polymerase II. *Nature* **558**, 318–323 (2018).
46. G. L. Dignon, W. Zheng, Y. C. Kim, R. B. Best, J. Mittal, Sequence determinants of protein phase behavior from a coarse-grained model. *PLoS Comput. Biol.* **14**, e1005941 (2018).
47. F. G. Quiroz, A. Chilkoti, Sequence heuristics to encode phase behaviour in intrinsically disordered protein polymers. *Nat. Mater.* **14**, 1164–1171 (2015).
48. M. Hondele *et al*., DEAD-box ATPases are global regulators of phase-separated organelles. *Nature* **573**, 144–148 (2019).
49. S. E. Reichheld, L. D. Muiznieks, F. W. Keeley, S. Sharpe, Direct observation of structure and dynamics during phase separation of an elastomeric protein. *Proc. Natl. Acad. Sci. U.S.A.* **114**, E4408–E4415 (2017).
50. T. Yuwen, J. P. Brady, L. E. Kay, Probing conformational exchange in weakly interacting, slowly exchanging protein systems via off-resonance $R_{1\rho}$ experiments: Application to studies of protein phase separation. *J. Am. Chem. Soc.* **140**, 2115–2126 (2018).
51. T. Yuwen *et al*., Measuring solvent hydrogen exchange rates by multifrequency excitation ^{15}N CEST: Application to protein phase separation. *J. Phys. Chem. B* **122**, 11206–11217 (2018).
52. M. P. Hughes *et al*., Atomic structures of low-complexity protein segments reveal kinked β sheets that assemble networks. *Science* **359**, 698–701 (2018).
53. S. Rauscher, R. Pomès, The liquid structure of elastin. *eLife* **6**, e26526 (2017).
54. J. Klein-Seetharaman *et al*., Long-range interactions within a nonnative protein. *Science* **295**, 1719–1722 (2002).
55. C. Dai, W. Gu, p53 post-translational modification: deregulated in tumorigenesis. *Trends Mol. Med.* **16**, 528–536 (2010).
56. H. Jung, C. G. Gkogkas, N. Sonenberg, C. E. Holt, Remote control of gene function by local translation. *Cell* **157**, 26–40 (2014).
57. M. L. Nosella, J. D. Forman-Kay, Phosphorylation-dependent regulation of messenger RNA transcription, processing and translation within biomolecular condensates. *Curr. Opin. Cell Biol.* **69**, 30–40 (2021).
58. Z. Monahan *et al*., Phosphorylation of the FUS low-complexity domain disrupts phase separation, aggregation, and toxicity. *EMBO J.* **36**, 2951–2967 (2017).
59. A. A. Labokha *et al*., Systematic analysis of barrier-forming FG hydrogels from Xenopus nuclear pore complexes. *EMBO J.* **32**, 204–218 (2013).
60. A. M. Blokhuis *et al*., Comparative interactomics analysis of different ALS-associated proteins identifies converging molecular pathways. *Acta Neuropathol.* **132**, 175–196 (2016).
61. T. Zarin *et al*., Proteome-wide signatures of function in highly diverged intrinsically disordered regions. *eLife* **8**, e46883 (2019).
62. I. Pritišanac, T. Zarin, J. D. Forman-Kay, A. M. Moses, Whence blobs? Phylogenetics of functional protein condensates. *Biochem. Soc. Trans.* **48**, 2151–2158 (2020).
63. P. J. Flory, Themodynamics of high polymer solutions. *J. Chem. Phys.* **10**, 51–61 (1942).
64. M. L. Huggins, Some properties of solutions of long-chain compounds. *J. Phys. Chem.* **46**, 151–158 (1942).